

Voltammetric behaviour of LMO at the nanoscale: a map of reversibility and diffusional limitations

E.M. Gavilán-Arriazu* [a],[b], M.P. Mercer [c],[d], D.E. Barraco [b], H.E. Hoster [c],[d] and E.P.M. Leiva* [a]

[a] Dr. E.M. Gavilán-Arriazu and Prof. E.P.M. Leiva
Departamento de Química Teórica y Computacional
Facultad de Ciencias Químicas, Universidad Nacional de Córdoba,
INFIQC, Córdoba, Argentina
E-mail: maxigavilan@hotmail.com
E-mail: ezequiel.leiva@unc.edu.ar

[b] Dr. E.M. Gavilán-Arriazu and Prof. D.E. Barraco
Facultad de Matemática, Astronomía y Física,
IFEG-CONICET
Universidad Nacional de Córdoba Córdoba, Argentina

[c] Dr. M.P. Mercer and Prof. H.E. Hoster
Department of Chemistry,
Lancaster University, Bailrigg,
Lancaster, United Kingdom

[d] Dr. M.P. Mercer and Prof. H.E. Hoster
ALISTORE European Research Institute
CNRS FR 3104, Hub de l'Energie, 80039 Amiens, France

Supporting information for this article is given via a link at the end of the document

Abstract: Understanding and optimization of single particle rate behaviour is normally challenging in composite commercial lithium-ion electrode materials. In this regard, recent experimental research has addressed the electrochemical Li-ion intercalation in individual nanosized particles. Here, we present a thorough theoretical analysis of the Li⁺ intercalation voltammetric behaviour in single nano/micro-scale LiMn₂O₄ (LMO) particles, incorporating realistic interactions between inserted ions. A transparent 2-dimensional zone diagram representation of kinetic-diffusional behaviour is provided that allows rapid diagnosis of the reversibility and diffusion length of the system dependent on particle geometry. We provide an Excel file where the boundary lines of the zone diagram can be rapidly recalculated by setting input values of the rate constant, k^0 and diffusion coefficient, D . The model framework elucidates the heterogeneous behaviour of nanosized particles with similar sizes but different shapes. Hence, we present here an outlook for realistic multiscale modelling of real materials.

Introduction

By now, lithium ion (Li-ion) batteries are well optimized in terms of capacity, proving successful in portable electronics, electric vehicles and potentially even stationary storage [1–5]. On the other hand, the key factors governing the rate performance of the electrodes are not fully understood. In particular, a proper description of Li-ion intercalation in nanosized materials is of primary importance for battery electrode design to inform how size and geometry impact on rate performance and lifetime. Most research has been focused on the behaviour of composite electrodes, where the contribution of particles with different sizes and shapes, together with the influence of agglomeration and the binder, plays an important role [6,7]. This approach circumvents analysis of single particle behaviour because the contribution of each particle to the total behaviour results in a collective average in electrochemical responses.

The spinel cathode LiMn₂O₄ (LMO) presents a good rate performance, moderate theoretical capacity and high abundance,

potentially making this chemistry suitable for stationary storage applications. However, in spite of the previous extensive research on composite microsized particles used in commercial cathodes [8,9], the redox behaviour of individual nanosized particles practically remains a virtually unexplored research area.

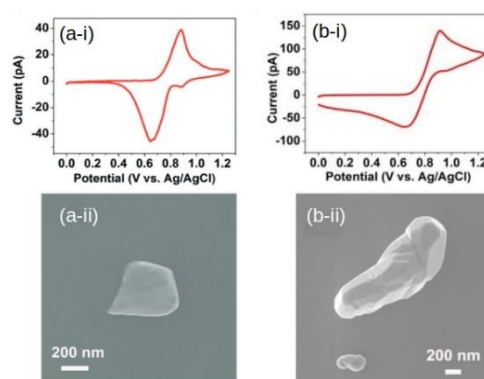


Figure 1. Cyclic voltammograms (i) for particles a and b, with the corresponding SEM images (ii). Reproduced with permission from reference [10], John Wiley & Sons Copyright © 2011. CC BY 4.0.

Remarkably, LMO ensembles of nanosized particles have been found to exhibit higher reversibility and better performance than the micrometric counterpart, but the origin of this improvement was not clear [11]. The recent work of Tao et al. [10], set a precedent by measuring cyclic voltammograms for individual LiMn₂O₄ particles of nanometric size using scanning electrochemical cell microscopy (SECCM), getting well resolved voltammetric features at scan rates as high as 1 V/s. Two cyclic voltammograms from this work, (a-i) and (b-i), for individual particles and the

RESEARCH ARTICLE

corresponding SEM images, (a-ii) and (b-ii), are shown in Figure 1. Contrasting behaviours can be observed concerning the shape of the voltammograms, due to the different shape of the particles.

In this way, they showed how particle size and geometry determine the current response for (de)intercalation of Li ions into LMO. The work suggests substantial unexplored headroom for systematic performance optimization via tuning of the particle geometry. Dynamic models are needed to 1. understand the relationship between voltammetric features and single particle geometry and 2. decouple the influence of charge transfer versus the finiteness of diffusion on those features.

In principle, the interplay between charge transfer-kinetics and diffusion in the voltammetry finite systems has been analyzed by Aoki et al.^[12] using zone diagrams as discussed below. However, that simple analysis lacks one fundamental feature: the interaction between inserted ions, which results into two voltammetric components instead of the single one observed in the non-interacting formulation of reference^[12].

Vassiliev et al.^[13] made a first attempt to improve this modelling by introducing the interaction between the ions using a Frumkin-type isotherm approach. On a similar basis, we developed preliminary work on the voltammetric responses of LiMn_2O_4 half cells with single sized particles ranging from the nanometric to the micrometric scale^[14]. We found that this approach was useful to show that particle size and geometry are relevant for electrochemical intercalation of Li^+ in electrode materials. However, coming close to the experimental situation of a more rigorous formulation of the interaction between the inserted ions is necessary and this is one of the achievements of the present work.

The (de)intercalation of Li ion from/into the electrodes is more complex than a Langmuir-intercalation isotherm (non-interacting) or even Frumkin-intercalation isotherm^[12,15], because: (I) interactions between Li ions, and between Li and the host, play a key role^[16–19] (II) the interactions are more complex than those of the classical Frumkin-intercalation isotherm and vary with the cell's state of charge (SOC)^[20–23] and (III) during (de)intercalation, order-disorder transitions take place that necessitate a more advanced description of the entropic terms than those of an ideal solid solution^[24–26], which is assumed in continuum level descriptions such as the Doyle-Fuller-Newman (DFN) model^[27]. Therefore, to simulate numerical voltammograms, the interaction terms between the inserted ions need to be carefully considered dependent on state of charge^[20–23].

Going back to charge transfer kinetic-diffusion interplay mentioned above, it must be recognized that zone diagrams^[28] may provide a faster diagnostic criterion than straightforward simulation under different operating conditions. Thus, the formulation of zone diagrams with realistic interaction between inserted ions appears to be necessary and this is the subject of this work.

So, the present work provides an essential improvement compared to our previous modelling, via a) a more physically realistic description of the intercalation isotherm, correctly capturing the order disorder/transition in the LMO system while including SOC-dependent interaction and b) a thorough zone diagram analysis^[12,28–30]. The latter construction provides a straightforward guide to experimentalists on the ranges of nanoparticle sizes where different kinetic/diffusional regimes expected, depending on the sweep rates used.

To the best of our knowledge, no zone diagrams to perform kinetic/diffusional analysis like those presented here, have been previously constructed to analyze Li ion intercalation.

Since the present model attempts to simulate single particle systems, some experimental factors will not be considered: (I) the current for the charge and discharge of the double layer capacitance at the interface, (II) side reactions like decomposition of the binder, (III) local modifications on the electrolyte concentration, (IV) particle aggregation.

Computational Methods

The voltammetric current resulting from a controlled potential sweep, say cyclic (CV) or linear sweep voltammetry (LSV), reflects the thermodynamic and kinetic events arising during the reduction and oxidation reactions upon lithium ion insertion/deinsertion. A complete basic description of a voltammetric experiment must consider two main aspects: the principles of diffusion and the electrode/electrolyte interface kinetics. Concerning the former aspect, we followed the procedure described in references^[13,14] that we shortly revisit in the Supplementary Information (SI), section S1.

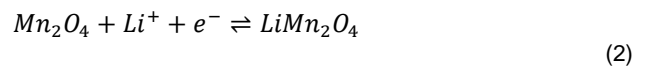
Concerning the interfacial electrode/electrolyte kinetics, we will use the popular Butler-Volmer approach relating the faradaic current i and the overpotential $\eta = E(t) - E^0(x)$, where $E(t)$ is the working electrode potential respect to Li / Li^+ and $E^0(x)$ is the equilibrium potential that is function of the Li^+ occupation x :

$$i(E) = Q\{x(0, t) e^{(1-\alpha)f\eta} - [1 - x(0, t)]e^{-\alpha f\eta}\} \quad (1)$$

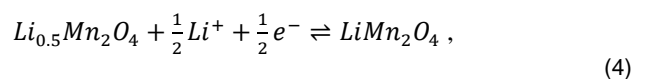
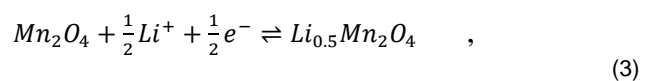
In this expression, $x(0, t)$ is the Li^+ occupation at the electrode surface, α the transfer coefficient, $Q = SF(\rho n_{\text{Li}}/M_r)k^0$ where F is Faraday constant, S the surface area, n_{Li} the fraction of intercalated Li^+ associated with each intercalation step (voltammetric peak), here $n_{\text{Li}} = 0.5$, M_r the molecular mass, ρ the phase density and k^0 the heterogeneous rate constant; $f = F/RT$, where R is the gas constant and T the temperature.

An important improvement in the present work with respect to previous ones^[13,14] is the modelling of $E^0(x)$ with an adequate thermodynamic background, using a lattice-gas Mean-Field (MF) approximation, which considers the energy changes during Li^+ (de)intercalation due to the host contraction or expansion. The thermodynamic aspects of the present model are inspired by the work of Gao et al.^[24], and is explained below.

The global reaction equation for Li^+ intercalation in manganese oxide to yield LiMn_2O_4 can be written as follows:



and it occurs in two steps:



In the first step, Equation (3), with the lattice being initially empty, half of the tetrahedral 8a sites of the spinel LiMn_2O_4 become occupied by Li ions. In a potential sweep, this step becomes evident as a first cathodic peak. In the second step, Equation (4), sweeping the potential negatively, the other half of the 8a sites are filled with Li ions and a second cathodic peak appears. On further reduction, the material converts into $\text{Li}_2\text{Mn}_2\text{O}_4$, which is of no interest for the present work.

To model the previously described insertion phenomena, we adopted in our previous work^[31] a two component Frumkin isotherm taken from the literature^[13], that was found useful to understand a number of features of the voltammetric behavior of the present system. However, that approach to modelling the isotherm and voltammogram was an approximation, because each of the two components were assumed to fill independently of one another. More accurate models consider the effect of interactions between the two components, as shall be further detailed below. In order to obtain a quantitative description, we switch from such model to a lattice-gas Bragg-Williams (Mean-Field) approach.

With this purpose, we briefly revisit previous models^[17,24,26,32,33] that have provided a satisfactory description of thermodynamic properties, like the order-disorder transition found in these systems and the changes observed in the electrochemical response when the Mn atoms from the 16d sites from the LMO structure are replaced by Li ions. These are features neglected in the two-component Frumkin isotherm approach presented earlier. It is known that Li^+ intercalation sites form a diamond structure with two laterally separated *fcc* sublattices. These sublattices will be denominated 1 and 2, respectively; with N sites on each of them, being x_1 and x_2 the degrees of occupation, with $0 \leq x_1, x_2 \leq 1$. The total occupation is calculated from:

$$x = \frac{x_1 + x_2}{2}. \quad (5)$$

We consider pairwise interactions with four of the first nearest neighbors of the same sublattice and twelve second nearest neighbors of the other sublattice. So, the Gibbs free energy of the lattice is written as:

$$G/N = U(x_1 + x_2) + 4J_1x_1x_2 + 6J_2x_1^2 + 6J_2x_2^2 - T(S_1 + S_2)/N \quad (6)$$

where U is the interaction energy between the host lattice and the guest Li ion, J_1 and J_2 are the two-body interactions between the first nearest Li neighbours and the second-nearest Li neighbours, respectively, T is the temperature and the S_i is the configurational entropy of sublattice i . Gao et al.^[24] assumed fixed interaction parameters with state of charge. However, to account for the experimentally-observed difference in peak height and half width between the two peaks it is important to account for changes in these parameters with lithium occupation, x , as shown below and discussed in detail in other works^[24,26,32].

After taking the derivative of Equation (6) with respect to x_1 and x_2 and using Stirling approximation, the MF chemical potential for sublattices 1 and 2 is:

$$\mu_1 = U + 4J_1(x)x_2 + 12J_2(x)x_1 + 4\frac{\partial(J_1(x))}{\partial x_1}x_1x_2 + 6\frac{\partial(J_2(x))}{\partial x_1}x_1^2 + 6\frac{\partial(J_2(x))}{\partial x_1}x_2^2 - k_B T \ln\left(\frac{1-x_1}{x_1}\right), \quad (7)$$

$$\mu_2 = U + 4J_1(x)x_1 + 12J_2(x)x_2 + 4\frac{\partial(J_1(x))}{\partial x_2}x_1x_2 + 6\frac{\partial(J_2(x))}{\partial x_2}x_1^2 + 6\frac{\partial(J_2(x))}{\partial x_2}x_2^2 - k_B T \ln\left(\frac{1-x_2}{x_2}\right), \quad (8)$$

where U is the interaction between a Li ion and the whole lattice, $J_1(x)$ and $J_2(x)$ are the interaction energies with the first and second nearest neighbors, respectively. In previous treatments J_1 and J_2 were treated as independent of x . Within the approach presented here, we will consider the energy variations due to the host modifications during Li^+ (de)intercalation; this is known as elastic energy^[24,26,32]. In the present model, we have allowed for the variation of energy $J_2(x)$ with Li^+ occupation. These are defined as:

$$J_1(x) = J_1^0, \quad (9)$$

$$J_2(x) = J_2^0 + \frac{B}{[1 - e^{-\delta(x-x_0)}]}(x - x_0), \quad (10)$$

In these formulations J_1^0 and J_2^0 are considered constant values, B is the slope of a straight line describing a linear change of $J_2(x)$ with lattice occupation when $x > x_0$. The factor $1/(1 - e^{-\delta(x-x_0)})$, with $x_0 = 0.5$, is a switch function that allows the change of $J_2(x)$ from constant value to a linear relationship with x . This variation represents the change of $J_2(x)$ due to the expansion of the lattice cell parameter upon intercalation^[34]. On the other hand, $J_1(x)$ is considered to have a constant value because a repulsive energy value fixes the peak separation when representing the derivative of the isotherm, as was studied in previous work^[26].

At equilibrium $\mu_1 = \mu_2 = \mu$. So, given a chemical potential $\mu = -E/e$, where E is the working electrode potential vs Li/Li^+ and e the elementary charge. Equations (7) and (8) can be solved iteratively to compute x_1 and x_2 . For such purpose, we used the multivariable Newton-Raphson method^[35].

To test the insertion MF isotherm we first use the same parameters $J_1^0 = 37.5$ meV, $J_2^0 = -4$ meV, $U = -4.12$ eV at $T = 298$ K, as those used in reference^[32], varying the new parameter B with $x_0 = 0.5$ and $\delta = 50$. Figure 2a shows the change of $J_2(x)$ variation with x , for different values of B . The main features of the function are highlighted in the figure. We assumed that B is positive, since the lattice expands as lithium is inserted inside the host, as observed experimentally^[34,36]. In the present notation, a positive energy value represents a repulsive interaction term while a negative one represents an attractive one. Figures 2b and c show how the isotherm and the derivative of the isotherm changes as B is modified, respectively. When $B = 0$ meV, we have the same case as that of Reference^[32], i.e, without elastic energy, and two symmetric peaks are observed in the derivative of the isotherm. Then, as B increases, the peak at higher voltages decreases, while the peak at lower voltages remains unaltered. This is so because, as B is larger, when $x > x_0$, the energetic change as the Li ions are inserted in the electrode is higher, thus, the interaction energy $J_2(x)$ becomes gradually less attractive due to lattice expansion. This is manifest in a smaller increase of the lattice occupation with electrode potential as B is larger. The results are in agreement with the qualitative features observed in experimental measurements^[36-38].

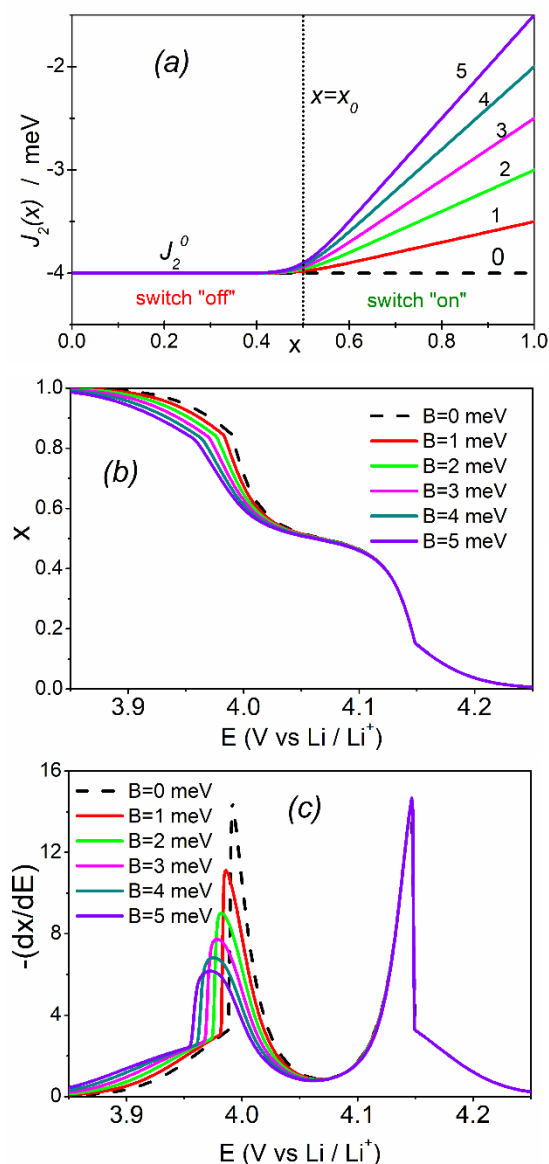


Figure 2. a) Changes of the energy for a pair of Li ions as given in Equation (10), due to the host modification. Switch "on" and "off" make reference to the switch of this function when $x = x_0$. The values of the slope B in meV are detailed above the lines. b) Calculated MF isotherm. c) negative values of the derivative of the isotherms of Figure b.

Results and Discussion

The insertion isotherm modelled in the previous section was used to model the equilibrium voltammetric profile and fitted to the experimental LMO data of Schlueter et al. [26]. The thermodynamic parameters J_1^0 , J_2^0 , U and B for Equations (7)-(10) were obtained using the Nelder-Mead simplex [39,40] to fit the occupations as a function of potential obtained at a very low charging rate [26]. The result for the isotherm fit is shown in Figure 3a. The fitted values of the parameters are shown in Table 1. As observed in Table 1, the values of the parameters obtained are similar to those used in previous modelling [26,32]. Figure 3b shows the typical pair of peaks

observed in the electrochemical measurements due to the 2-step filling of the LMO 8a sites with Li-ions. Since the present system contains two types of (physically equivalent) sites with the transition emerging from inter-ion interactions, the current from Equation (1) is calculated by adding two current contributions, as explained in the SI, section S2.

Table 1. Best fit parameters used to obtain the theoretical curve presented in Figure 3.

Parameter	Value
J_1^0 [meV]	28.1425
J_2^0 [meV]	-3.4639
B [meV]	6.03563
U [meV]	-4.093.927

In order to simulate voltammetric curves under non-equilibrium conditions, choices must be made for the parameters d (particle radius or diffusion length), T (temperature), D (diffusion coefficient) and k^0 (rate constant). To make a first qualitative test of the performance of the model, the kinetic parameters $D = 3.1622 \times 10^{-10} \text{ cm}^2 \cdot \text{s}^{-1}$ and $k^0 = 1.71 \times 10^{-6} \text{ cm} \cdot \text{s}^{-1}$, and the average particle radius $d = 0.4 \text{ } \mu\text{m}$, were adopted using parameters obtained from the experimental measurements from reference [37], as described in detail in SI, section S3. Note that the choice of $d = 0.4 \text{ } \mu\text{m}$ corresponds to an average particle size of $0.8 \text{ } \mu\text{m}$, while the authors of reference [39] reported a bimodal distribution with effective particle diameters 0.25 and $1.3 \text{ } \mu\text{m}$. We performed test runs with these two particle sizes, see Figure S2, finding that the voltammograms obtained with all these diameters show the same trends as the experimental ones. Simulated voltammetric curves (Figure 4) were obtained with the parameters listed in Table 2. As observed, the intercalation capacitance, $C = i/v$, obtained with our model, shows the same trends as those observed in the experimental case (presented in the insets of Figure 4). Interfacial kinetic control is found for the set of sweep rates listed in the top panel (Figure 4a), while diffusional control is dominant for the sweep rates listed in the bottom panel (Figure 4b). This change of regime with increasing sweep rate is typical for intercalation systems [41].

Table 2. Parameters used in simulations of the voltammetric profiles of Figure 3.

Parameter	Value
D [$\text{cm}^2 \cdot \text{s}^{-1}$]	3.1622×10^{-10}
k^0 [$\text{cm} \cdot \text{s}^{-1}$]	1.71×10^{-6}
d [μm]	0.4
T [K]	298
ρ [$\text{g} \cdot \text{cm}^{-3}$]	4.281
n_{Li}	0.5
M_r [$\text{g} \cdot \text{mol}^{-1}$]	180.8
α	0.4

Aoki et al. [12] have found that the voltammetric behaviour of a simple electrochemical reaction in a finite diffusion space can be classified with two dimensionless parameters:

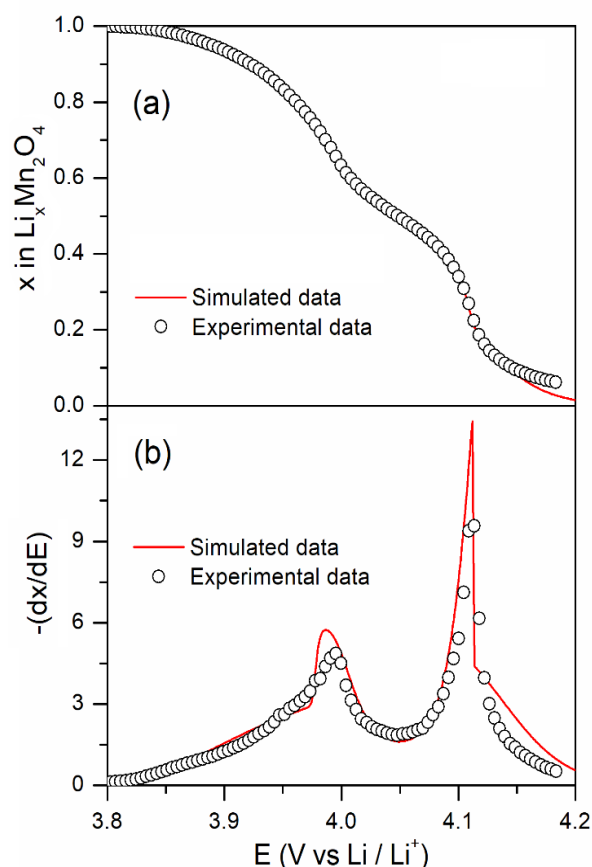


Figure 3. a) Best fit (red continuous line) of the experimental occupation vs potential curve (small circles) taken from the data from reference [26] with permission from the Royal Society of Chemistry. CC BY 3.0. Best fit parameters are given in Table 1. The root square mean error (RSME) calculated was 0.010134. b) Voltammetric curve for quasi-equilibrium conditions. The red curve was obtained using parameters obtained from the fitting of the isotherm and the circles are experimental data reproduced from [26] with permission from the Royal Society of Chemistry. CC BY 3.0.

$$\Lambda = k^0(RT/nFDv)^{1/2}, \quad (11)$$

$$w = nFv d^2/RTD. \quad (12)$$

where Λ is a kinetic parameter also known as reversibility coefficient [42], while w is a finite diffusion parameter.

On the basis of this framework, we will analyze in the following the voltammetric behaviour of LMO under surface kinetics/diffusion control by constructing a dimensionless zone diagram with the parameters of Equations (11) and (12), using the realistic intercalation isotherm that we derived for LMO as input. The zone diagrams, which represent the kinetic parameters in equations 11-12 in a $\log(\Lambda)$ - $\log(w)$ plane, illustrate in two dimensions the impact of the degree of reversibility of the electrochemical surface reaction and the finiteness of diffusion on the intercalation process [28]. This is the first time that this kind of zone representation has been applied to Li^+ intercalation, and we also report for the first time on the use of a mean field approach to describe non-equilibrium voltammetry features for any Li-ion system, here specifically for LMO.

Concerning charge transfer kinetics, it is well known that an electrochemical reaction is denominated reversible if it follows the

Nernst equation [42]. The degree of reversibility of charge transfer at the electrode/solution interphase varies depending on operating conditions, principally the mass transfer conditions and the time scale of the experiment. For example, a reaction is considered to be irreversible in a voltammetric experiment if the charge transfer is very slow as compared with the rate at which the potential is swept, because little time is given for the forward and backward reactions to equilibrate [43,44]. An intermediate behaviour between these limits is considered to be a quasi-reversible reaction.

Complementary to the charge transfer reaction, mass transport due to diffusion arises when a concentration gradient is established close to the electrode surface, where charge transfer occurs. The finiteness of the diffusion depends on the characteristic length along which the species have to spread. For example, if the diffusion layer thickness is such that the changes of the concentration profile never reach the total length of the system, the diffusion is considered to be semi-infinite. If the changes of the concentration profile reach the limits of the system, we are dealing with finite diffusion. Finally, when the potential perturbation is so slow that that a concentration gradient is practically not established along the system, the behaviour of the

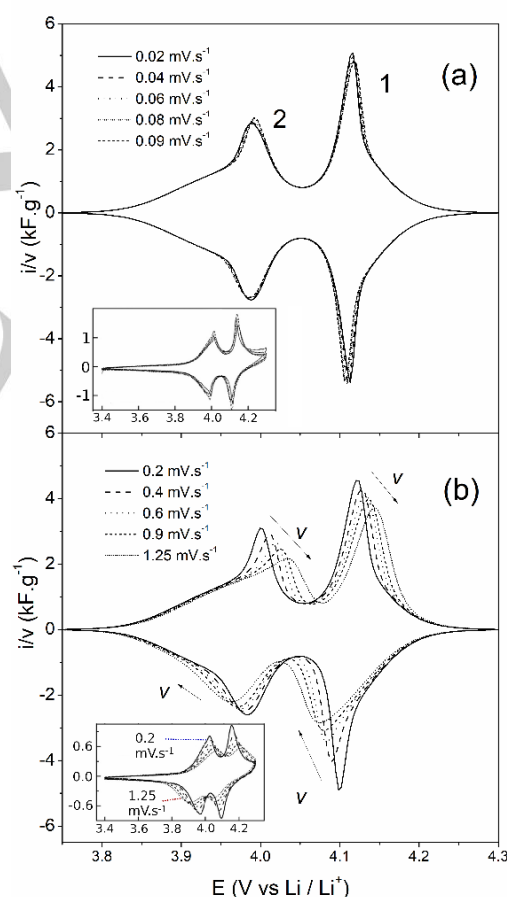


Figure 4. Results for a set of voltammograms simulated at different sweep rates. The results show the same trend as those the reference [37] using 1 M LiClO_4 in EC and DEC (1:1) as electrolyte. The insets are reproduced with permission from reference [37], Copyright 2011 Elsevier B.V. Black arrows denote the decrease of the current peak for larger sweep rates. The redox couple at higher voltages was labelled as 1, while the redox couple at lower potentials was labelled as 2. The axis labels in the insets correspond to those of the main figures.

RESEARCH ARTICLE

system is classified as that of a surface wave [12]. It is clear that both features, reversibility and diffusion, are intrinsically linked and depend on the operating conditions of the experiment [44], therefore they have an influence on the behaviour of the voltammetric current.

To give the reader a first flavor of the results discussed in detail below, we illustrate in Figure 5, the four limiting cases of charge transfer/diffusion control obtained for a non-interacting kinetics (Figure 5a) and for the present system (Figure 5b): reversible surface waves, irreversible surface waves, reversible semi-infinite diffusion, irreversible semi-infinite diffusion. As it can be seen, the nature of the interaction between the inserted ions (Figure 5b) is necessary to reproduce the features of the experimental system, LMO in this case. As shown in the Figure, the interactions between lithium ions in the system cause the voltammetric feature to split into two peaks, for a reversible surface wave. These two peaks can be attributed to ordering of lithium within the host. Because of the Li^+ - Li^+ interactions, lithium preferentially fills one type of site until the lattice is half full (right hand peak), and then filling of the other half of the sites proceeds (left hand peak). The effect of semi-infinite diffusion and/or charge transfer limitations has qualitatively similar effects on the voltammogram. On visual inspection, it is also difficult to distinguish the irreversible regimes with and without interactions between the lithium atoms. This necessitates a kinetic description that can more objectively delineate the boundaries between diffusion or charge transfer limitation, or a mixed regime, based on voltammetric features for a system with interactions.

In a more comprehensive approach and following reference [12], the degree of reversibility of the intercalation reaction at the electrode interface is classified here as: reversible (*R*), quasi-reversible (*QR*) and irreversible (*I*). Concerning the finiteness of the Li^+ diffusion, the regimes will be classified into surface waves or thin-film diffusion (*S*), finite diffusion (*F*) and semi-infinite diffusion (*SI*). The diffusional regimes (*S*, *F* and *SI*) are denoted by super-indexes. A schematic view of a zone diagram is

represented in Figure 6a. Thus, each section of the zone diagram refers to different combinations of the degree of reversibility and the finiteness of the diffusion, where the voltammetric parameters presents specific features. Therein, for example, a zone denoted with QR^{SI} indicates a quasi-reversible reaction and a semi-infinite diffusion space.

To construct the zone diagram for LMO, we adopted overall the approach of reference [12]. A deviation of 3% of the peak current with respect to different limiting cases (as those shown in Figure 5) observed in different regions of the zone diagram. The details are rather involved, strictly methodological and deserve meticulous reading. For this reason, we treat this point in detail in the Supplementary Information, section S4. There we explain carefully the limiting behaviours of the current in each of the zones of the diagram.

Since we have here two voltammetric couples instead of one, as in reference [12], unless otherwise stated, we have to choose one of the peaks for the diagnosis. We decided to use the first cathodic (intercalation) peak (redox couple 1 in Figure 4), because the second intercalation peak (redox couple 2 in Figure 4) is highly affected by the diffusional tail of redox couple. For more details see SI, section S4.

The zone diagram plots were constructed for planar diffusion conditions and are presented in Figure 6a. A comparison of the present results with those where the interactions between the inserted ions are ignored (i.e. a non-interacting intercalation isotherm, shown by a grey dotted line), shows that the border lines of the mean field zone diagram (red dashed line) are shifted with respect to the non-interacting case. This is emphasized in the figure, showing with grey arrows how these shifts occur, and commented below.

The horizontal red line for LMO, corresponding to the *R* – *QR* and *QR* – *I* borders shift with respect to the grey line. This effect is more pronounced for *R* – *QR* than for *QR* – *I*. This indicates that the voltammogram for LMO is more sensitive to charge transfer limitations than it would be if there were no interactions in the

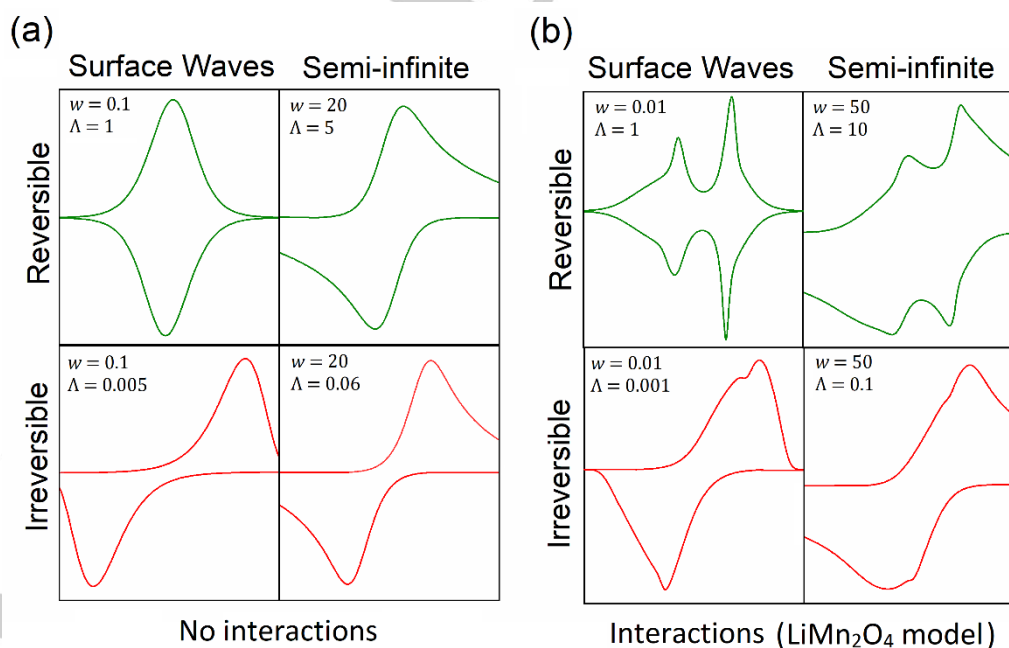


Figure 5. Illustration of limiting cases for a non-interacting system (a) and for LMO as modelled in the present work (b). The corresponding w and Λ used are detailed above each voltammogram.

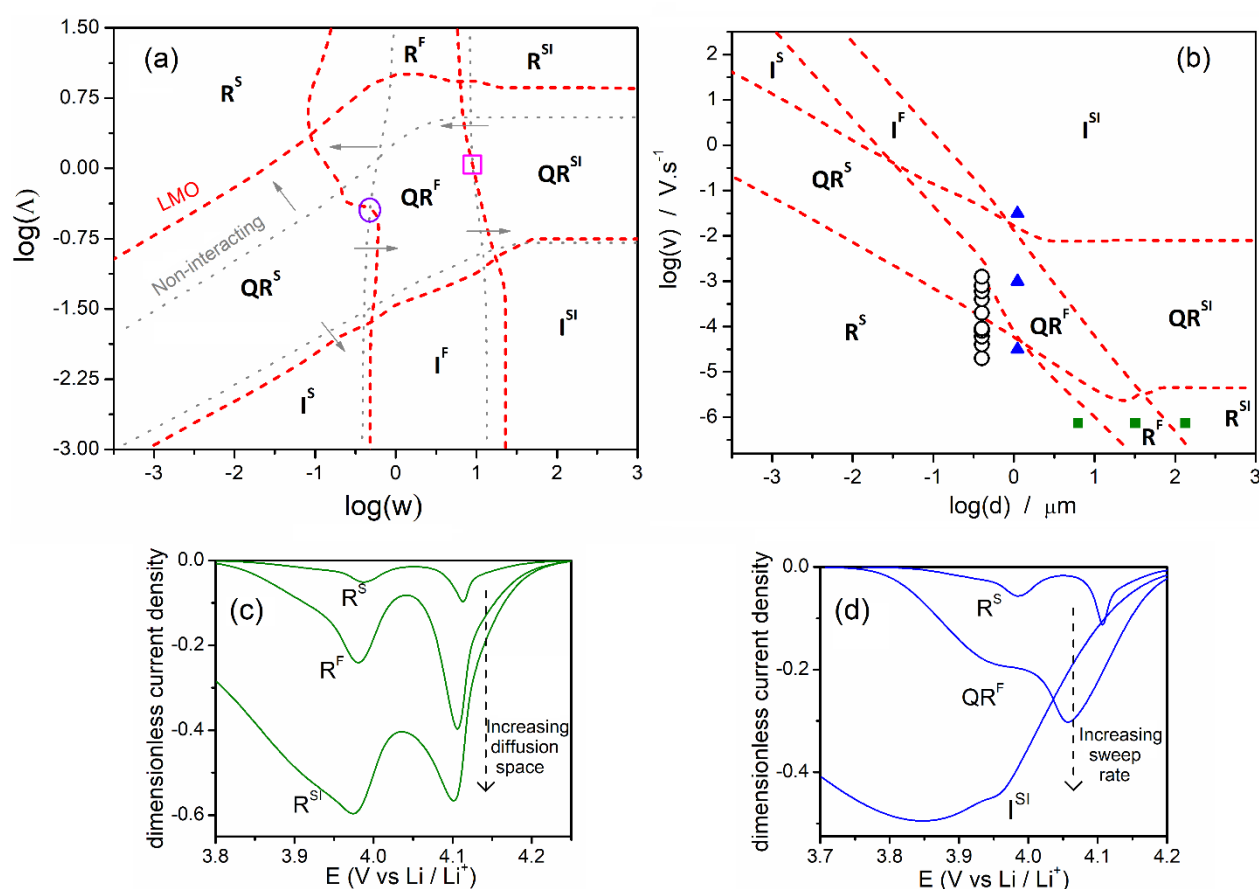


Figure 6. a) Dimensionless zone diagram representation, using the present mean field approximation to describe the thermodynamics of Li-ion insertion in LMO (red dashed lines). The zone diagram with non-interacting conditions is represented by grey dotted lines, and was constructed according to the criteria discussed in reference [12]. The symbols denote different cases as follows: *R* (reversible), *QR* (quasi-reversible), *I* (irreversible), *S* (surface waves), *F* (finite size diffusion), *SI* (semi-infinite diffusion). b) $\log(\text{sweep rate})$ - $\log(\text{distance})$ representation for LMO using diffusion coefficients and heterogeneous rate constant calculated from the experimental data from reference [37]. White circles correspond to experimental conditions for voltammograms of Figure 4. c) sample reductive linear sweep voltammograms corresponding to the green squares drawn in the zone diagram of Figure b). d) sample reductive linear sweep voltammograms corresponding to the blue triangles drawn in the regions of the zone diagrams b).

system, i.e. the system is in a charge transfer limited regime at lower sweep rates than if no interactions were present.

Regarding finiteness of diffusion, the diagram for LMO is also displaced as compared with the non-interacting case. The difference between LMO with interactions and the non-interacting isotherm is most noteworthy at the boundary between a surface wave (superscript *S*) and finite diffusion (superscript *F*) in the reversible and quasi-reversible regimes. The transition to finite diffusion occurs at much smaller particle size for LMO than the non-interacting case. These results suggest a pronounced effect of system ordering in LMO on diffusion when the system is not limited by charge transfer.

For the limit between surface waves and finite diffusion above to the point marked with a violet circle in the figure, the LMO line shifts to the left of the grey line. On the contrary, below the violet circle, the border line is slightly shifted to the right of the grey diagram. This change of behaviour with respect to the non-interacting case is observed when the pair of peak currents, distinguishable above the violet circle, merge into a single peak below this point. The same occurs with the line that separates *F* and *SI* zones, around the point marked with a pink square.

Now, if specific values for the kinetic parameters D and k^0 are assumed, the $\log(\Delta)$ - $\log(w)$ representation may be turned into a sweep-diffusion length ($\log(v)$ - $\log(d)$) diagram, which is more straightforward to compare with experimental data. The values of

D and k^0 presented in Table 2, corresponding to electrolyte composition 1 M LiClO₄ in EC and DEC (1:1), were used to plot the zone diagram shown in Figure 6b. Figures 6c and d show some examples of voltammograms in different zones of the diagram, at constant sweep rate (green squares in Figure 6b) and particle radius (blue triangles in Figure 6b), respectively. The corresponding zone diagram for each voltammogram is labelled at the bottom of the current response.

This new type of zone diagram is useful to easily make some qualitative predictions. Let us insert in Figure 6b the operating conditions of Zheng [37], simulated above in Figure 4. These working conditions are shown as white circles in the diagram of Figure 6b. It can be noted how, as sweep rate increases, the system passes from a reversible surface wave zone (R^S) to a quasi-reversible surface wave zone (QR^S), and finally to a quasi-reversible finite diffusion zone (QR^F). This means that the changes observed in the shape of the voltammograms in Figure 4 are mainly due to variations in the charge transfer kinetics, rather than to diffusional limitations; although the last two points fall in the QR^F zone. Thus, this type of representation allows a straightforward determination of the kinetic and diffusional limitations for Li⁺ insertion in LMO.

Moreover, the representations can easily be adapted to different electrolyte compositions just by changing the kinetic parameters k^0 , since the diffusion coefficient D is determined by the electrode

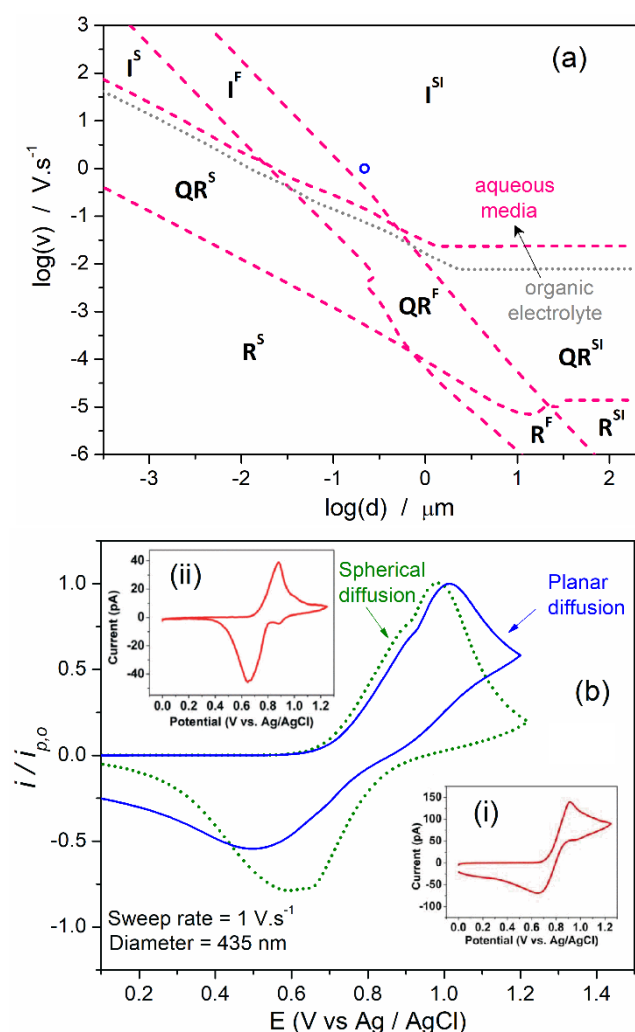


Figure 7. a) Zone diagram for LMO in aqueous media. b) Simulated voltammograms normalized with respect to the oxidative peak current ($i_{p,o}$) for planar (blue) and spherical (green) diffusion, using the same kinetic and diffusional parameters as those used to represent the blue dot in Figure 7a. The insets i) and ii), corresponding to Figure 1(a-i) and Figure 1(b-i) respectively, show experimental voltammograms, reproduced with permission of [10]. John Wiley & Sons Copyright © 2011. CC BY 4.0.

material rather than the electrolyte. Two common solvents used for the electrochemical Li^+ intercalation in LMO are organic solvents, like 1 M LiClO_4 in EC and DEC (1:1), and aqueous media. So, it is expected that different $\log(v) - \log(d)$ zone diagrams emerge in each case. Taking $k^0 = 3 \times 10^{-6} \text{ cm.s}^{-1}$ for aqueous media with 1M Li_2SO_4 as electrolyte [45], we thus constructed the zone diagram shown in Figure 7a. The grey dotted line shows one of the lines of the zone diagram for the organic electrolyte, to emphasize the shift with respect to the aqueous media line (pink dashed lines). The white circle with blue borders in Figure 7a shows the location in the diagram corresponding to a LMO particle of volume $4.5 \times 10^{-14} \text{ cm}^3$, a typical size found in the measurements of reference [10], with a sweep rate of 1 V.s^{-1} . The point lies in the I^{SI} region, but close to the border line with the I^F zone. With particles of this size, the system could rapidly shift to a finite diffusion behaviour with a small decrease in the sweep rate. This fact could explain the variety of voltammetric responses observed in the ensemble of particles.

$\log(v) - \log(d)$ zone diagrams for other systems may be easily obtained using the Excel file "ZDconstructor.xlsx" as explained in SI, section S5.

We performed simulations for finite systems having the same experimental conditions of that of the white circle with blue borders in Figure 7a, but with different particle shapes, with voltammograms represented in Figure 7b. While the blue voltammogram corresponds to planar diffusion (corresponding to the blue dot in Figure 7a), the green curve is a simulation for a spherical particle.

We go back now to the experimental conclusions of Tao et al. [10], which largely motivated the present work. Tao et al. found that the morphologies of the LiMn_2O_4 particles showed considerable variations throughout the ensemble. Differences in voltammetric peak shapes and positions were attributed to intrinsic differences between the LiMn_2O_4 particle morphologies. Simulated results therefore seem to support the findings of Tao et al. that particle morphology influences the voltammetric behaviour of individual LMO particles, and moreover the simulations deliver a possible explanation for the findings. In particular, the insets of Figure 7b show two typical responses taken from reference [10] (the same as those shown in Figure 1), labelled with ii) and i). As pointed out above, contrasting behaviours can be observed: while inset i) presents peaks with a typical diffusional tail, inset ii) shows narrower peaks. The blue curve indicates, by a longer diffusional tail after the peak current, characteristic of planar diffusion. On the other hand, the steeper current drop of the green curve is characteristic of spherical diffusion. The simulated results suggest that the LMO particle from the inset i) is governed by a planar diffusion, while particle from ii) is under spherical diffusion conditions. However, a further consideration on the SECCM technique is due before claiming for agreement between experiment and the present simplified modeling. One of the merits of the SECCM experimental arrangement is that the pipettes used in this setup possess a conical geometry, so that mass-transport down the probe is predominantly governed by quasi-radial diffusion [46]. This results in the fact that (near) steady-state conditions can be achieved when using probes on nanoparticles with a relatively smaller radius. However, for larger particles the diffusional pattern may become more complicated, and diffusion in solution could become the limiting process. The latter phenomenon is not included in the present modeling and further research is needed to make a clear assessment.

In future work, the simulation accuracy could be improved further, allowing the framework to be applied to other systems. This could be achieved by accounting for 1. anisotropic diffusion and 2. differences in k^0 depending on face of the nanoparticle into which the ions are being inserted.

Finally, to show the potential of the present approach to interconnect different simulation scales, we make some comments on how this strategy could be inserted into a more general multi-scale modelling (MSM) [47] framework. A possible scheme is shown in Figure 8. The model used in the present work is marked with red borders lines boxes and arrows, surrounded by a red ellipse. A proposed multi-scale scheme, in which the actual model is inserted, is represented with black dashed border lines and arrows. The present model lacks the dependence of the diffusion coefficient and k^0 on the state of charge, and this information may be obtained from kinetic Monte Carlo simulations (kMC), as illustrated in the middle of the figure. The energy barriers for diffusion and (de)intercalation of Li^+ (from) into the

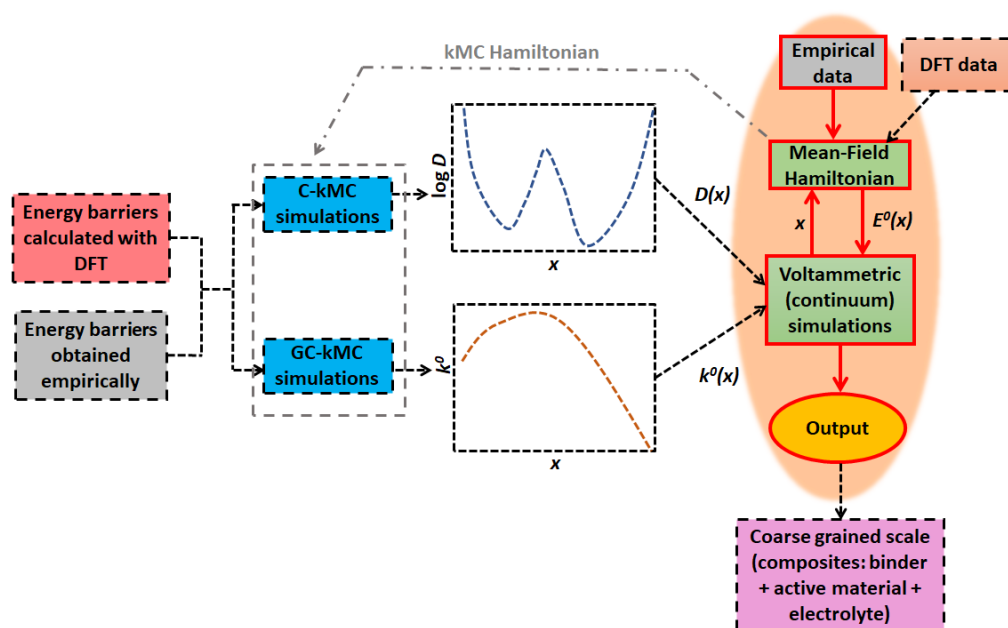


Figure 8. An example of an MSM scheme where the present simulation tool (red cloud) could be introduced. Different scales are represented with different colours: red for first principle calculations, light blue for atomistic scale, green for continuum and lilac for coarse grained scale.

electrode required for the kMC simulation, could be estimated with DFT and / or empirical data^[48,49] (left of the figure). This information would be fed into the kMC model, to study the changes of D with x in a canonical ensemble (C-kMC) and the variations of k^0 with the state of charge in a Grand Canonical ensemble (GC-kMC). For an example of this procedure see references^[19,21,50] or the review paper of reference^[51] devoted to kMC applied to Li-ion batteries and post Li-ion batteries. The latter information would be used in voltammetric simulations: given a state of charge from CV, the program reads the values of $D(x)$ and $k^0(x)$ to calculate the current.

The mean-field Hamiltonian could be alternatively modelled from density functional theory (DFT) calculations or from empirical data and used as input for kMC. This is illustrated by a grey dash-dotted arrow going from the mean-field Hamiltonian to C-kMC and GC-kMC simulations.

Outside of the “output” box, the scheme of Figure 8 captures only aspects related to the inserted ions. A coarse grained scale (lilac box at the end of the scheme) would be useful to add the other aspects of the composite, like binder, active material, electrolyte, agglomeration, etc. The introduction of the present scheme into a pseudo-two-dimensional model like that presented in reference^[52] would be straightforward.

Conclusions

We have presented here a thorough theoretical analysis of the voltammetric behaviour for the intercalation of Li^+ in nanosized-microsized LiMn_2O_4 using a novel approach for the interaction between inserted ions, which improves the thermodynamic description of the insertion phenomenon through an atomistic mean field description. This work provides the first application of this description in the continuum approach adapted from earlier work by Aoki et al., naturally decoupling the relative rates of diffusion and charge transfer. The different zones on the diagram allow the relative rates of diffusion and charge transfer to be

determined dependent on the system size. The original representation requires dimensionless parameters, so we instead transfer the diagram into a representation of sweep rate and system size. In this way, the voltammetric regime of the system (considering electrochemical reversibility and diffusion length) can easily be predicted in terms of these two parameters. At the same time, the model framework rationally explains what the evolution of features from cyclic voltammetry of Li ions actually means, in terms of changes to particle geometry or sweep rate. We also provided a tool to construct different sweep rate-length zone diagrams by setting k^0 and D . In this way, researchers can apply the model to different experimental setups.

The present work also leaves a message for the manufacturers of composite electrodes, concerning the need to control the geometry and the shape of the particles. The fine structure of particles plays a role in the degree of reversibility and transport of Li^+ . The framework presented here demonstrates how, and moreover provides a strategy to determine this information based on voltammetric features. For example, as shown in the simulations, spherical particles are less prone to diffusional control, for similar particle sizes, so it would be desirable to tune the synthesis conditions to promote spherical morphology. As expected, it would also be desirable to reduce the particle size, but there is a practical limit because smaller particles present higher surface areas and, thus, less stable interfaces. The boundaries in the zone diagrams show the maximum particle size regime that, for example, avoids electrochemical irreversibility under the relevant experimental time scales, thus allowing a more rational decision on particle size for the intended application.

Even greater predictive accuracy could be attained, for example, by i) determining the most energetically favourable surface facets for a given particle size and also ii) accounting for different charge transfer rates on those different nanoparticle surface facets.

Lastly, we highlighted the potential use of the present simulation tool in multi-scale modelling (MSM), that aims to provide reliable theoretical information linking models of different hierarchies. For

this aim, we showed a scheme as a tentative example of how this model can be implemented in MSM.

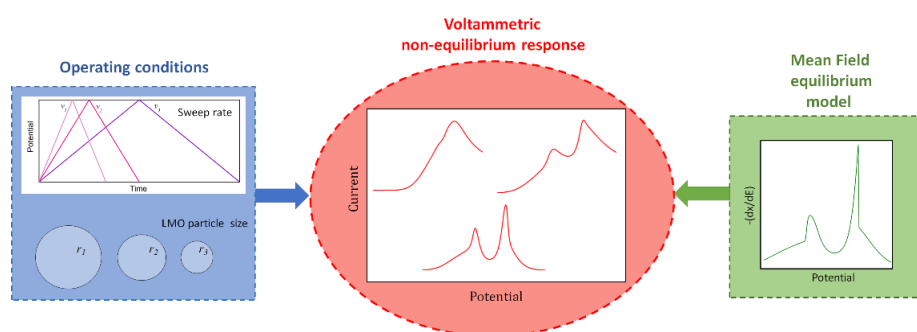
Acknowledgements

E.P.M. Leiva acknowledges grants PIP CONICET 11220150100624CO, PUE/2017 CONICET, FONCYT PICT-2015-1605 and SECyT of the Universidad Nacional de Córdoba. Support by CCAD-UNC and GPGPU Computing Group, Y-TEC and an IPAC grant from SNCAD-MinCyT, Argentina, are also gratefully acknowledged. E.M. Gavilán-Arriazu acknowledges Manuel López Galván for helpful mathematical suggestions.

Keywords: Lithiation • Cyclic voltammetry • Intercalations • Electrochemistry • LMO

- [1] V. Etacheri, R. Marom, R. Elazari, G. Salitra, D. Aurbach, *Energy Environ. Sci.* **2011**, *4*, 3243–3262.
- [2] J. B. Goodenough, Y. Kim, *Chem. Mater.* **2010**, *22*, 587–603.
- [3] M. R. Palacín, *Chem. Soc. Rev.* **2009**, *38*, 2565–2575.
- [4] B. Scrosati, J. Hassoun, Y. K. Sun, *Energy Environ. Sci.* **2011**, *4*, 3287–3295.
- [5] X. Zeng, M. Li, D. Abd El-Hady, W. Alshitari, A. S. Al-Bogami, J. Lu, K. Amine, *Adv. Energy Mater.* **2019**, *9*, 1–25.
- [6] H. Berg, J. O. Thomas, *Solid State Ionics* **1999**, *126*, 227–234.
- [7] W. Tang, X. Yang, Z. Liu, S. Kasaishi, K. Ooi, *J. Mater. Chem.* **2002**, *12*, 2991–2997.
- [8] S. B. Tang, M. O. Lai, L. Lu, *Mater. Chem. Phys.* **2008**, *111*, 149–153.
- [9] F. Cheng, H. Wang, Z. Zhu, Y. Wang, T. Zhang, Z. Tao, J. Chen, *Energy Environ. Sci.* **2011**, *4*, 3668–3675.
- [10] B. Tao, L. C. Yule, E. Daviddi, C. L. Bentley, P. R. Unwin, *Angew. Chemie - Int. Ed.* **2019**, *58*, 4606–4611.
- [11] L. Hernán, J. C. Arrebola, A. Caballero, J. Morales, *J. Nanomater.* **2008**, 1–10.
- [12] K. Aoki, K. Tokuda, H. Matsuda, *J. Electroanal. Chem.* **1984**, *160*, 33–45.
- [13] S. Y. Vassiliev, E. E. Levin, V. A. Nikitina, *Electrochim. Acta* **2016**, *190*, 1087–1099.
- [14] E. M. Gavilán-Arriazu, M. P. Mercer, O. A. Pinto, O. A. Oviedo, D. E. Barraco, H. E. Hoster, E. P. M. Leiva, *J. Solid State Electrochem.* **2020**, DOI 10.1007/s10008-020-04717-9.
- [15] M. Levi, D. Aurbach, *Electrochim. Acta* **1999**, *45*, 167–185.
- [16] M. D. Levi, E. a. Levi, D. Aurbach, *J. Electroanal. Chem.* **1997**, *421*, 89–97.
- [17] M. P. Mercer, S. Finnigan, D. Kramer, D. Richards, H. E. Hoster, *Electrochim. Acta* **2017**, *241*, 141–152.
- [18] E. M. Gavilán-Arriazu, O. A. Pinto, B. A. L. de Mishima, E. P. M. Leiva, O. A. Oviedo, *J. Electrochem. Soc.* **2018**, *165*, A2019–A2025.
- [19] E. M. Gavilán-Arriazu, O. A. Pinto, B. A. López De Mishima, D. E. Barraco, O. A. Oviedo, E. P. M. Leiva, *Electrochim. Acta* **2020**, *331*, DOI 10.1016/j.electacta.2019.135439.
- [20] E. V. Vakarín, J. P. Badiali, *J. Phys. Chem. B* **2002**, *106*, 7721–7724.
- [21] E. M. Gavilán-Arriazu, M. P. Mercer, O. A. Pinto, O. A. Oviedo, D. E. Barraco, H. E. Hoster, E. P. M. Leiva, *J. Electrochem. Soc.* **2020**, *167*, 13533.
- [22] M. P. Mercer, M. Otero, M. Ferrer-Huerta, A. Sigal, D. E. Barraco, H. E. Hoster, E. P. M. Leiva, *Electrochim. Acta* **2019**, *324*, 134774.
- [23] M. P. Mercer, C. Peng, C. Soares, H. E. Hoster, D. Kramer, *J. Mater. Chem. A* **2021**, *9*, 492–504.
- [24] Y. Gao, J. N. Reimers, J. R. Dahn, *Phys. Rev. B* **1996**, *54*, 3878–3883.
- [25] S. Il Pyun, S. W. Kim, *J. Power Sources* **2001**, *97–98*, 371–376.
- [26] S. Schlueter, R. Genieser, D. Richards, H. E. Hoster, M. P. Mercer, *Phys. Chem. Chem. Phys.* **2018**, *20*, 21417–21429.
- [27] M. Doyle, T. F. Fuller, J. Newman, *J. Electrochem. Soc.* **1993**, *140*, 1526–1533.
- [28] J. M. Savéant, K. B. Su, *J. Electroanal. Chem.* **1984**, *171*, 341–349.
- [29] Y. S. Kim, V. Balland, B. Limoges, C. Costentin, *Phys. Chem. Chem. Phys.* **2017**, *19*, 17944–17951.
- [30] D. J. Martin, B. D. McCarthy, E. S. Rountree, J. L. Dempsey, *Dalt. Trans.* **2016**, *45*, 9970–9976.
- [31] E. M. Gavilán-Arriazu, M. P. Mercer, O. A. Pinto, O. A. Oviedo, D. E. Barraco, H. E. Hoster, E. P. M. Leiva, *J. Solid State Electrochem.* **2020**, DOI 10.1007/s10008-020-04717-9.
- [32] S. Pyun, S. Kim, *Mol. Cryst. Liq. Cryst. Sci. Technol.* **1999**, *155–162*.
- [33] R. Darling, J. Newman, *J. Electrochem. Soc.* **1999**, *146*, 3765–3772.
- [34] M. Bianchini, E. Suard, L. Croguennec, C. Masquelier, *J. Phys. Chem. C* **2014**, *118*, 25947–25955.
- [35] D. Britz, *Digital Simulation in Electrochemistry*, Berlin, Heidelberg, **2005**.
- [36] T. Ohzuku, M. Kitagawa, T. Hirai, *J. Electrochem. Soc.* **1989**, *136*, 3169.
- [37] J. P. Zheng, D. J. Crain, D. Roy, *Solid State Ionics* **2011**, *196*, 48–58.
- [38] M. D. Chung, J. H. Seo, X. C. Zhang, A. M. Sastry, *J. Electrochem. Soc.* **2011**, *158*, A371.
- [39] Y. Huang, W. F. McColl, *Proc. IEEE Int. Conf. Syst. Man Cybern.* **1996**, *3*, 1702–1705.
- [40] M. S. Caceci, W. P. Cacheris, *Byte* **1984**, *9*.
- [41] A. K. Hjelm, G. Lindbergh, A. Lundqvist, *J. Electroanal. Chem.* **2001**, *506*, 82–91.
- [42] A. J. Bard, L. R. Faulkner, *Electrochemical Methods: Fundamentals and Applications*, **2001**.
- [43] H. Angerstein-Kozłowska, J. Klinger, B. E. Conway, *J. Electroanal. Chem.* **1977**, *75*, 61–75.
- [44] R. Seeber, C. Zanardi, G. Inzelt, *ChemTexts* **2016**, *2*, DOI 10.1007/s40828-016-0027-3.
- [45] C. Erinmwingbovo, V. Siller, M. Nuñez, R. Trócoli, D. Brogioli, A. Morata, F. La Mantia, *Electrochim. Acta* **2020**, *331*, DOI 10.1016/j.electacta.2019.135385.
- [46] C. L. Bentley, *Electrochem. Sci. Adv.* **2021**, 1–18.
- [47] A. A. Franco, *RSC Adv.* **2013**, *3*, 13027–13058.
- [48] C. Peng, M. P. Mercer, C. K. Skylaris, D. Kramer, *J. Mater. Chem. A* **2020**, *8*, 7947–7955.
- [49] B. Xu, S. Meng, *J. Power Sources* **2010**, *195*, 4971–4976.
- [50] E. M. Gavilán-Arriazu, O. A. Pinto, B. A. López de Mishima, D. E. Barraco, O. A. Oviedo, E. P. M. Leiva, *Electrochem. commun.* **2018**, *93*, 133–137.
- [51] E. M. Gavilán-Arriazu, M. P. Mercer, D. E. Barraco, H. E. Hoster, E. P. M. Leiva, *Prog. Energy* **2021**, *3*, 042001.
- [52] A. Jokar, B. Rajabloo, M. Désilets, M. Lacroix, *J. Power Sources* **2016**, *327*, 44–55.

Entry for the Table of Contents



Thermodynamic (mean field) and kinetic modeling is used to analyse lithium insertion into LMO electrodes of different sizes, using cyclic voltammetry at different sweep rates. A map of reversibility and diffusional limitations is constructed. This modeling is relevant to understand and predict the voltammetric behaviour of single particles of this system at different size and time scales, and may also be of interest for multiscale modeling.